Tamminen, Aleksi; Pälli, Samu-Ville; Ala-Laurinaho, Juha; Aspelin, Arthur; Oinaanoja, Akseli; Taylor, Zachary

Holograms with neural-network backend for submillimeter-wave beamforming applications

Published in:
SPIE Conference Proceedings

DOI:
10.1117/12.2557754

Published: 01/01/2020

Document Version
Publisher's PDF, also known as Version of record

PROCEEDINGS OF SPIE

SPIEDigitalLibrary.org/conference-proceedings-of-spie

Holograms with neural-network backend for submillimeter-wave beamforming applications

Tamminen, Aleksi, Pälli, Samu-Ville, Ala-Laurinaho, Juha, Aspelin, Arthur, Oinaanoja, Akseli, et al.

Aleksi Tamminen, Samu-Ville Pälli, Juha Ala-Laurinaho, Arthur Aspelin, Akseli Oinaanoja, Zachary Taylor, "Holograms with neural-network backend for submillimeter-wave beamforming applications," Proc. SPIE 11411, Passive and Active Millimeter-Wave Imaging XXIII, 114110C (23 April 2020); doi: 10.1117/12.2557754

SPIE.

Event: SPIE Defense + Commercial Sensing, 2020, Online Only

Holograms with neural-network backend for submillimeter-wave beamforming applications

Aleksi Tamminen, Samu-Ville Pälli, Juha Ala-Laurinaho, Arthur Aspelin,
Akseli Oinaanoja, and Zachary Taylor
Aalto University Department of Electronics and Nanoengineering, MilliLab
Maarintie 8, Espoo, 02150, Finland.

ABSTRACT

We present a new method to carry out localization based on distributed beamforming and neural networks. A highly dispersive hologram, is used together with a terahertz spectrometer to localize a corner-cube reflector placed in the region of interest. The transmission-type dielectric hologram transforms input pulse from the spectrometer into a complex pattern. The hologram causes complicated propagation paths which introduce delay so that different parts of the region of interest are interrogated in a unique way. We have simulated the emitted pulses propagating through the hologram. The hybrid simulation combines the finite-difference and physical optics methods in time domain and allows for evaluating the dispersion and directive properties of the hologram. The dispersive structure is manufactured of Rexolite and it has details resulting in varying delay from 1 to 19 wavelengths across the considered bandwidth. The spectrometer is configured in reflection mode with wavelets passing in to the region of interest through the hologram. A data-collecting campaign with a corner-cube reflector is carried out. The effective bandwidth for the localization is from 0.1 THz to 2.1 THz, and the measured loss is 57 dB at minimum. The collected data is used to train a fully-connected deep neural network with the known corner-cube positions as labels. Our first experimental results show that it is possible to predict the position of a reflective target in the region of interest. The accuracy of the prediction is 0.5-0.8 mm at a distance of 0.17 m.

Keywords: Hologram, localization, neural network, submillimeter-wave.

1. INTRODUCTION

The image-forming technologies used in submillimeter-wave real-time screening systems are based on electrical or mechanical beam scanning. Typically, there is a quasioptical arrangement with focal points on the target in the region of interest and on the sensor. The focal point on target is steered by scanning mechanics, such as presented in [1], [2]. Other active imaging systems apply sensor arrays with controllable phase-shifts that enable beam steering without large, moving physical elements. Phase shifts can also be applied post detection in multi-sensor systems [3]. Imaging systems that utilize complex mechanical solutions may have limited mean-time between failureand that necessary increase the system footprint. Imaging systems with electrical beam steering may include thousands of sensors operating phase-coherently. Although the cost of transceiver technology at millimeter waves has come down, thanks to mass production for telecommunications and automotive radar, the components and subsystems still remain prohibitively expensive; especially at higher millimeter and submillimeter wavelengths.

"Single-pixel camera" refers to technology where an imaging system relies on a single sensor that is then multiplexed to different modes to interrogate the target in specific ways. These modes can be created with masks that introduce spatial modulation into the illumination on the target. In optics, multiple masks can be created in fast succession by using spatial light modulators. Spatial modulation of light intensity is based on microelectromechanical mirror arrays or liquid-crystal devices. Spatial modulators have been demonstrated, at millimeter and submillimeter waves, , using photo-injected Fresnel-zone plate antenna [4]. There, beam steering is carried out as a single-mode process, i.e., a single diffraction-limited spot is scanned across the target and multiplexed in time as the scan proceeds. Imaging based on quasi-random illumination of the region of interest has been demonstrated at close range millimeter waves in [5]. The designs require control of the radiating aperture by high-intensity photonics aligned with the millimeter-wave optical axis. Standoff imaging at centimeter waves with quasirandom illumination on the target through metasurface antennas has also been reported [6]. There, the region of interest is illuminated in a complex way through resonant structures that each contribute

Passive and Active Millimeter-Wave Imaging XXIII, edited by David A. Wikner,
Duncan A. Robertson, Proc. of SPIE Vol. 11411, 114110C · © 2020 SPIE
CCC code: 0277-786X/20/$21 · doi: 10.1117/12.2557754

a mode to the illumination. The image reconstruction in this technique requires an accurate model of the radio-wave propagation path.

We present the first results of localization based on a dispersive structure and neural network. A dispersive, dielectric hologram distributes the pulse from terahertz emitter onto the field of view as a wavelet. The dispersion is achieved with varying electrical pathlengths in the hologram. The reflection back from the target is recorded at the detector on the optical axis. A thin-film beam splitter is used to optically collocate source and detector for a normal reflection measurement. Complex mapping of the time-domain content to a transverse location is carried out by a trained neural network.

2. DISPERSIVE TIME-DOMAIN SYSTEM

In the proposed localization method, the object is illuminated with a wavelet. A sketch of the proposed localization setup is shown in Figure 1. In our case, the system has single transceiver consisting of the emitter and detector of a terahertz time-domain spectrometer (THz-TDS). The radiation is directed towards the target through a transmission-type hologram, which has complex quasirandom surface relief. The target in the region of interest is detected as weighted sum of its spatial reflectivity map. Our localization method is based on the following assumption: If the illuminating field varies enough spatially within the wavelet envelope duration, the detected reflection will carry information of the spatial properties of the target. We have explored these concepts with THz-TDS as the technology allows for fast time-domain sweeps across corresponding wavelength range that cannot be achieved with, e.g., submillimeter-wave extenders operating in TE_{10}-waveguide mode. Additionally, the desired dispersive property can be realized with structures that scale as wavelength and sufficient dispersion of the radiated field can be achieved with practical few-millimeter-thick structures by using THz-TDS.

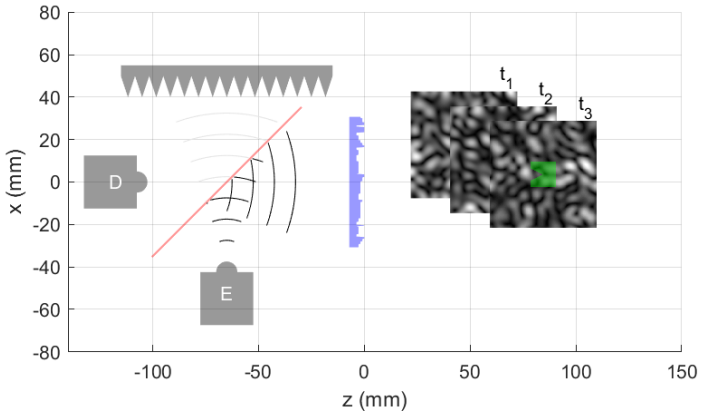

Figure 1. Quasioptical setup for localization task. The pulse from emitter (E) is directed towards the hologram (blue) with dielectric beam splitter (red). The wavelet disperses in the region of interest and the illumination on the target corner-cube reflector (green) varies as function of time. The spatial distribution of the incident energy in the region of interest is distinctly different from t_1 to t_3. The back-reflected wavelets are received at the detector (D) after propagating again through the hologram and beam splitter.

2.1 Terahertz time-domain spectrometer

The THz-TDS system is femtosecond-laser based spectrometer TeraSmart by Menlo Systems GmbH. The emitter and detector consist of antenna-coupled photoconductive switches. A strip-line antenna is used in the emitter and a dipole antenna is used in the detector [7]. The radiation is coupled through substrate-mounted silicon lens with clear aperture diameter of ~ 10 mm. Figure 2 shows the peak-normalized detected pulse in time- and frequency-domain when the emitter and detector are quasioptically coupled with a pair of plano-convex, dielectric lenses. The measured power spectral density falls into the noise floor just above 5 THz in this focused configuration. A band- and transform-limited model of the pulse is also shown with a noise-limited spectral content of 2 THz. The pulse model is used to simulate the performance of the dispersive structure and the 2 THz bandlimit is imposed to maintain reasonable simulation run times.

In addition to the focused configuration, a diverging configuration is evaluated. There, the focusing quasioptics are omitted and the emitter and detector are raster scanned facing each others. The scans cover a 72-mm by 72-mm area with 300-mm emitter-detector distance along the optical axis. Figure 3 a shows frequency-domain amplitude patterns from 0.1 to 2.1 THz. In a typical antenna measurement, the antenna under test is characterized with a probe antenna whose radiation

pattern is very accurately known. In our case, both the emitter and detector antennas are difficult to characterize over such large bandwidths, so the presented patterns include properties from the both. The patterns show above-noise performance up to 2.1 THz and demonstrate a clear main beam up to 350 GHz after which multi-lobe patterns appear. The minimum of the peak-normalized field in the scans is about −15 dB. The phase maps in Figure 3 b confirm a close-to spherical phase front throughout the frequency range.

The emitter and detector lie at 100 mm from the hologram in the final quasioptical setup, so the scanned area with −15-dB minimum corresponds to 24-mm by 24-mm area on the element. In terms of coupling a Gaussian beam (with radius of w) to the hologram, −15-dB level corresponds to $r = 1.72w$. The diameter of the hologram is $D = 61$ mm, which is approximately $D \approx 5w$ and almost all power from the emitter is incident on the hologram. As is evident from the measured patterns, they vary as function of frequency and the pattern can be described Gaussian only below 350 GHz. The variation especially above 350 GHz may be due to the inherently band-limited operation of the dipole and strip-line antennas. In our case, the multilobe pattern may be beneficial as it introduces additional dispersion. Figure 4 shows the peak-normalized, time- and frequency-domain field for locations where the measured pattern maximum is at 0.1, 0.6, 1.1, 1.6, and 2.1 THz. The spectral content is significantly different for different locations in the diverging configuration. The ratio of the pulse peak values is $|E_{\mathrm{d,pk}}|/|E_{\mathrm{f,pk}}| \approx 0.056$, corresponding to 25-dB loss due to the free-space propagation.

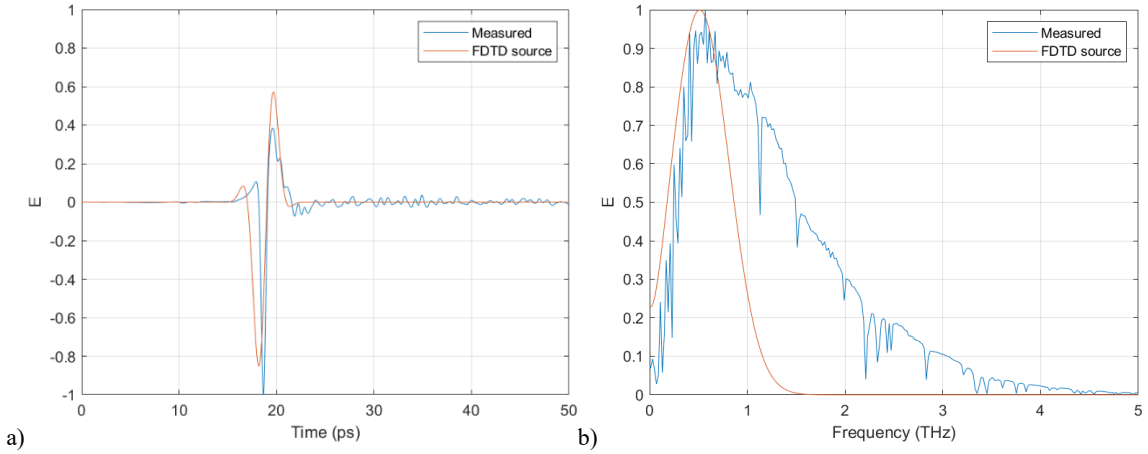

Figure 2. a) Measured (blue) and modeled (red) broad-band pulse from the THz-TDS. The modeled pulse is low-pass limited to approximately 1 THz in order to maintain reasonable FDTD simulation time. b) Frequency-domain representation of the pulses. The measurement is carried out with focusing quasioptics between the emitter and detector.

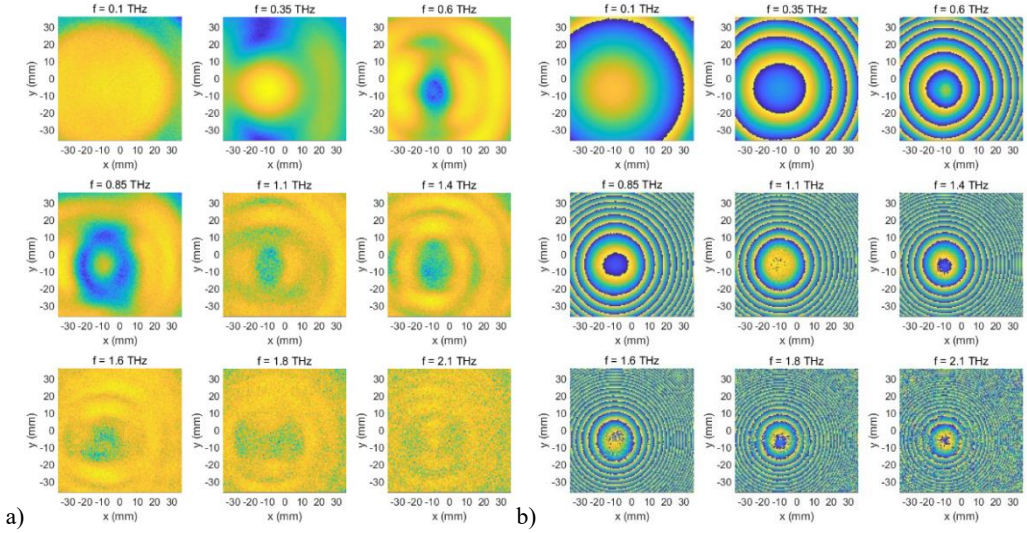

Figure 3. Detected pulse a) amplitude and b) phase in frequency-domain in the 72-mm by 72-mm raster scan at 300-mm on-axis distance.

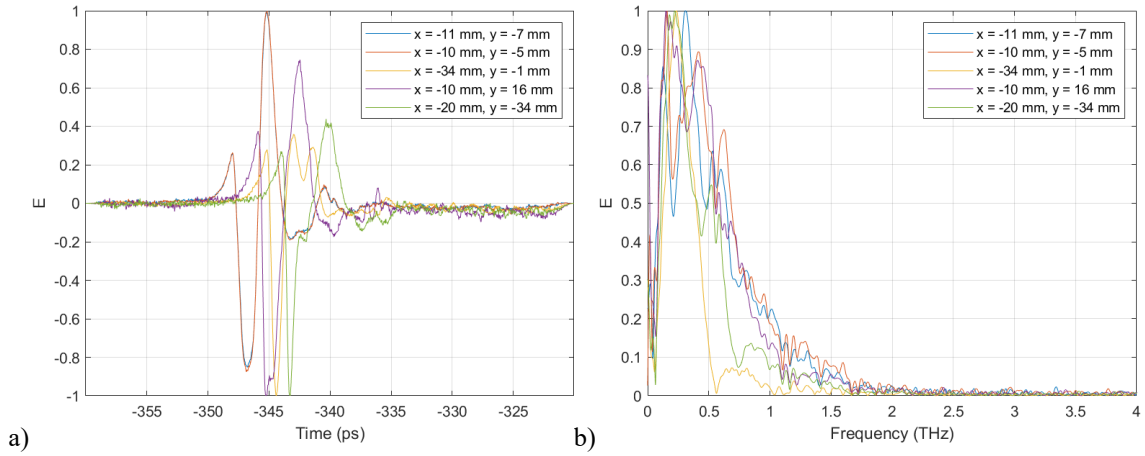

Figure 4. Measurements in diverging configuration: Normalized a) time- and b) frequency-domain representations of the detected pulse. The different curves are measurements at the peak-field locations at 0.1, 0.6, 1.1, 1.6, and 2.1 THz.

2.2 Dispersive element

The dispersive hologram is manufactured on 13-mm thick slab of cross-linked polystyrene (Rexolite 1422). The hologram transforms the incident pulse into a dispersive wavelet so that the field at the target is quasirandom and time varying. Figure 5 shows the cross section of the structure. The relative dielectric permittivity of Rexolite is $\varepsilon_r \approx 2.52 - j0.0005$ [8]. The step height of the surface relief is 1.68 mm, which equals to electrical path length from 0.9 to 18.7 wavelengths from 0.1 THz to 2.1 THz.

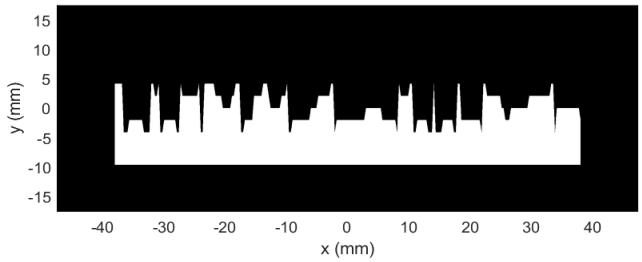

Figure 5. Cross section of the hologram.

Finite-difference time-domain simulations

The dispersive element is analyzed for the near-field effects with 2-dimensional finite-difference time-domain (FDTD) simulation. While the structure does not have symmetry allowing its operation to be fully characterized with 2D simulations, we carry out the simple simulation for an estimate of the expected dispersion for such surface relief. Further, the simulation explores the directivity of the dispersed wavelet towards the region of interest. The radiated field in the region of interest is calculated with time-domain physical optics (TD-PO) based on the FDTD results. Figure 6 shows the results of FDTD simulation for the cross section when $x = 0$ mm. The source in the simulation is as the modeled pulse in Figure 2 a. The simulation is run until the pulse is propagated through the dispersive element and the energy in the simulation model decayed to 0.1 % from its maximum value. The incoming pulse is modeled as a high-impedance source at $z = -17.5$ mm in the simulation domain. The pulse is delayed equal to a spherical propagation from x = 0 mm and $z = -106.6$ mm (source 100 mm behind the dispersive element). The simulation model is surrounded by perfectly matching layer and the radiated field propagating through $z = 17.5$ mm is used as radiating aperture in the TD-PO.

Figure 6 shows the simulated propagation through the hologram from 27 to 220 ps. The spherical pulse propagates through the smooth air-dielectric interface at 50 to 80 ps and 18 % of the energy reflects back to the emitter and detector. As the pulse propagates to the surface relief, scattering occurs at the dielectric-air interfaces. The scattering is non-isotropic with 70 % of the energy having been passing through the radiating aperture at $z = 17.5$ mm at ~ 170 ps. After that, isotropic propagation occurs for the small fraction of the energy. At 220 ps, the energy in the simulation domain is 9 % of the incident. The initial back reflection from the smooth surface on the back side of the hologram and the decaying isotropic

scattering likely reduce overall sensitivity. In some transceivers a high-isolation directional coupler is needed to separate the transmitter and the receiver. Using a beam splitter as a directional coupler may saturate the receiver and significantly limit sensitivity. Antireflection coatings on the hologram or a high-isolation directional coupler should improve our sensitivity as well.

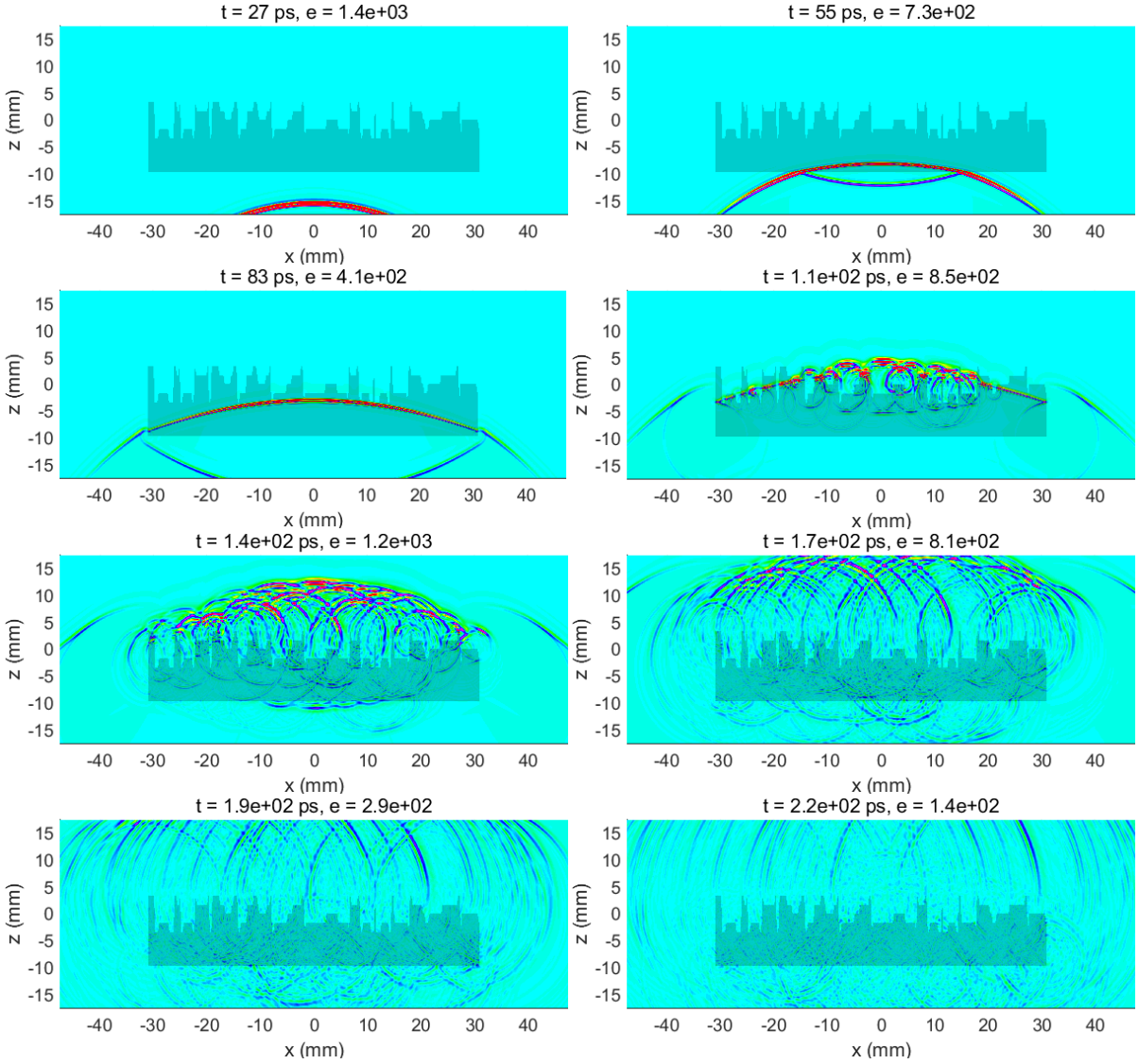

Figure 6. Snapshots of the FDTD simulation of the dispersive structure. Time increases ~ 30 ps from left to right and top to bottom. At the beginning, the pulse arrives at the back surface of the structure and partly reflects from it. Starting from $t = 83$ ps, the pulse interacts with the surface relief and scattering occurs. The total energy (e) in the simulation domain peaks at 140 ps and decays to 9 % of the maximum at 220 ps.

Time-domain physical-optics simulations

TD-PO is used to calculate the FDTD-simulated wavelet in the region of interest at $z = 167.5$ mm. In TD-PO, the current density at the boundary of the FDTD simulation domain is integrated in to the region of interest, where the dispersive property and the directivity of the structure is assessed. The time-domain physical-optics is as described in [8]-[11]. The equivalent surface current $\vec{J}$ at observation point is calculated as

$$\vec{J}(\vec{r},t) = \frac{1}{2\pi}\int_S \left[\frac{1}{R^2} + \frac{1}{Rc}\frac{\partial}{\partial\tau}\right]\vec{J}\left(\vec{r'},\tau\right) \times \hat{a}_R dS' \quad (1)$$

where $\vec{r}$ is the location in the region of interest and $\overrightarrow{r'}$ is the location in the FDTD radiation boundary. The distance between the two points is $R = \left|\vec{r} - \overrightarrow{r'}\right|$ and the contribution from each radiating FDTD element is delayed by $\tau = t - R/c$. The directional unit vector is $\hat{a}_R = \vec{r} - \overrightarrow{r'} / \left|\vec{r} - \overrightarrow{r'}\right|$.

Figure 7 a shows the simulation results on the x-axis at $z = 17.5$ mm over a 100 ps time window. The pulse propagates through the dispersive structure and appears at $z = 17.5$ mm at 150 ps. The wavelet is dispersed so that it decays 10 dB from its maximum value within 50 ps. The envelope of the original pulse from the source decays the same amount in only about 5 ps. The pulse is transformed to quasirandom wavelets that are approximately appearing to emanate from a single source point. Figure 7 b shows the TD-PO result in the region of interest at $z = 167.5$ mm. There, the pulse appears as wavelet that has most of its energy within 30-ps duration. Compared to the wavelet at the radiating aperture (Figure 7 a, $z = 17.5$ mm), the wavelet varies less as there is appreciable energy propagating outside the region of interest. More control on the direction of propagation could be possible with, e.g., a collimated feed. However, with this setup, we are limited in quasioptical arrangements due to maximum range limited by the THz-TDS intrinsic optical path and delay line. Finally, Figure 7 c shows the resulting time-domain fingerprints that are distinctly different for each location in the region of interest. Time is shown up to point where the energy in the simulation domain has decayed 99.9 %. In many cases the approximately single cycle pulse (plotted at 18.2 ps for comparison) has been transformed to a wavelet with 10-12 local extrema. We consider that in the practical measurements time window covering the wavelet up to about 700 ps in Figure 7 c is sufficient.

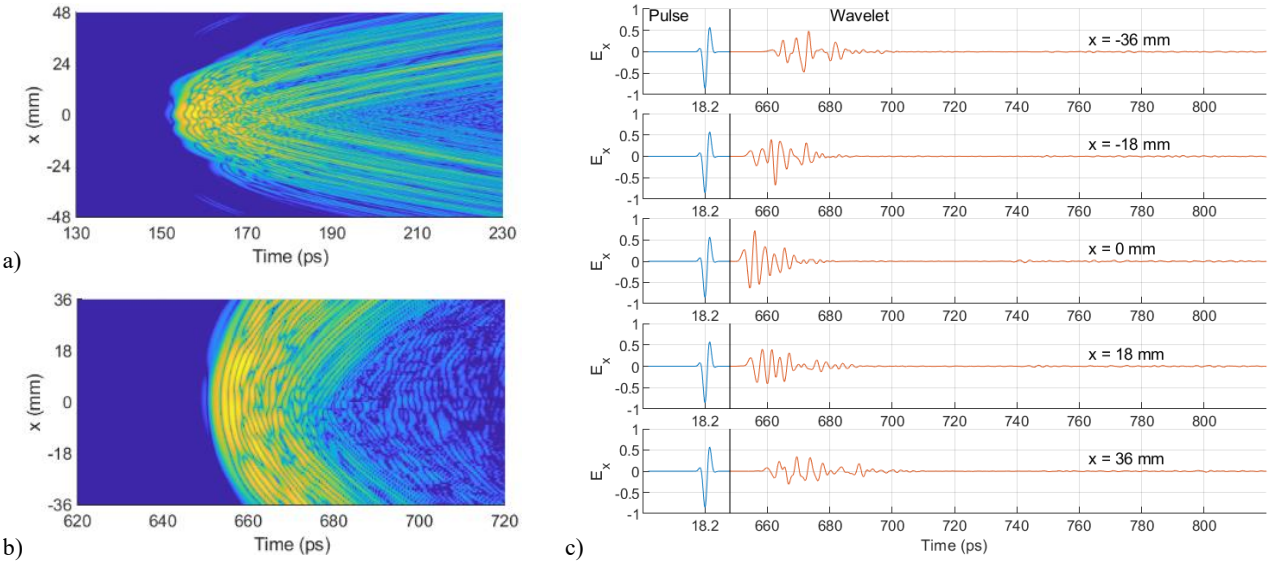

Figure 7. a) FDTD-simulated electric field at the perfectly matched layer (PML) boundary $z = 17.5$ mm as function of time. b) Electric field from FDTD is calculated in the region of interest at 167.5 mm with TD-PO. The field is normalized and the colormap is in logarithmic scale. c) Time-domain field (red) at different locations on the *x*-axis after the pulse has transmitted the dispersive element: the wavelet is spread at least 5 times compared to the original pulse from THz-TDS (blue), drawn next to the wavelet for comparison.

The presented 2D simulations indicate the general principles of operation with the hologram. In reality, the pulse propagation through the structure is more complex given the 3D shape. The hologram is manufactured via CNC techniques with estimated surface quality of few tens of micrometers. In addition to surface quality, the manufacturing process is limited by the available cutting tools (1 mm minimum diameter) that do not allow faithful realization of the designed complex structure. As a consequence, the deviations between designed and manufactured structure are considered unknown properties that are trained to the neural network.

3. LOCALIZATION WITH NEURAL-NETWORK

The dispersive structure is manufactured and installed in the quasioptical setup as is shown in Figure 8. The geometry of the setup is the same as described in Figure 1. A corner-cube reflector HR-127-5-AL from Spectrum Scientific Inc. is used

as the reflective target in the region of interest. The corner-cube diameter is 12.5 mm, so it roughly corresponds to the aperture of the anti-reflection-coated silicon lenses on the THz-TDS emitter and detector.

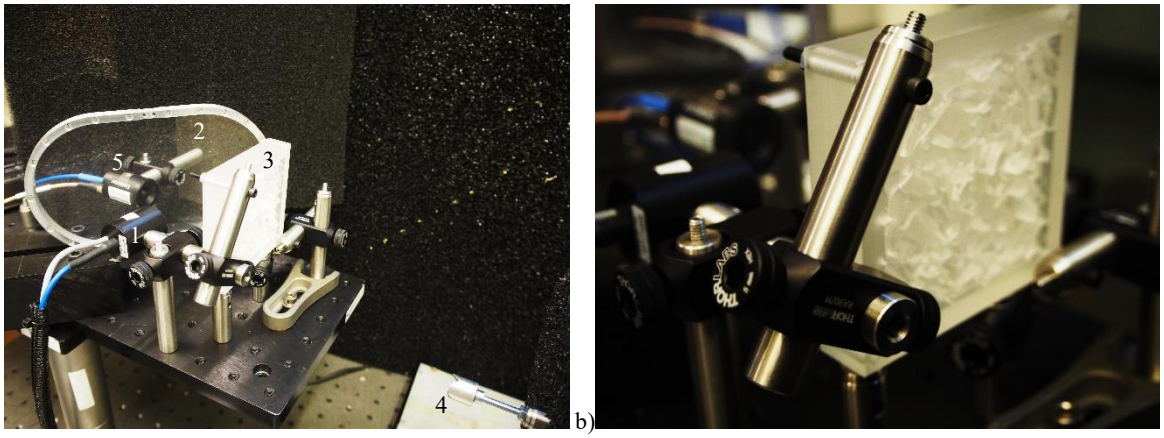

Figure 8. a) Quasioptical setup for the localization task: 1) emitter of the THz-TDS, 2) beam splitter, 3) hologram, 4) corner-cube reflector, and 5) detector of the THz-TDS. The corner-cube reflector is on a translational x-y stage. The surroundings and the background of the corner cube are lined with absorber. b) Close-up of the hologram installed in the quasioptics.

A link-budget analysis is completed to estimate the total loss in the setup. The detected pulse (wavelet) is recorded in three setups: 1) focused configuration corresponding to minimum path loss, 2) diverging configuration corresponding to the one-way free-space loss L_{fs} (25 dB), and 3) two-way configuration with the hologram and corner cube corresponding the full-system loss. The measured loss is tabulated in Table 1. The wavelet amplitude is recorded at the corner-cube position where peak amplitude is detected. The measured and calculated loss, both 57 dB, are well in line when we assume that the dielectric beam-splitter loss L_{bs} is 6 dB and the hologram loss L_{h} is 1 dB due to the reflections at the dielectric interfaces.

Table 1. Link budget for the two-way propagation with the corner cube in optimal position.

	Detected amplitude (V)	Measured loss (dB)	Loss components (dB)
Focused configuration	3.6	0	0
Diverging configuration	0.2	25	$L_{\mathrm{fs}} \approx 25$
Full system	0.005	57	$2L_{\mathrm{fs}} + L_{\mathrm{bs}} + L_{\mathrm{h}} \approx 50 + 6 + 1 = 57$

The data for the beamforming system is recorded as the detected wavelets when the corner-cube reflector is scanned in the region of interest. The scan area is 72-mm by 72-mm at $z \approx 167$ mm. Figure 9 a and b show the detected wavelets in x- and y-cuts of the scanned area. The emitted pulse transforms to wavelets with several local extrema spreading up to 30 ps in time (Figure 9 c). The detected wavelets amplitude is just above the noise floor at the edge of the scanned area. Prior to neural network training, the detected wavelets are low-pass filtered with cut-off frequency of 3 THz. The filtering limits the effect of noise and noise-like patterns on neural network convergence.

3.1 Neural network

A fully connected deep neural network is used in the localization task. The input data to the neural network is the detected wavelets that are normalized so that each has a peak value of $|E|_{\mathrm{pk}} = 1$. Also, the outputs of the neural network, x- and y-coordinates of the corner cube, are normalized to interval [0, 1]. The neural-network is developed with TensorFlow machine-learning platform through Python-based Keras API [12]. The input training data includes 20200 corner-cube locations in the region of interest and the number of activations (number of time-domain samples in single detected wavelet) in the input layer is 1381. The neural network is trained using Adam optimizer [13] with mean-squared error (MSE) as loss. The accuracy of the neural network is evaluated with input data from 249 corner-cube locations that are not shown to the network in training. The neural-network topography, as a printed Keras summary, is shown in Table 2. The activation function in the hidden layers is rectifying linear unit (ReLU). At the output, the activation function is sigmoid. There are 5728390 total trainable parameters in the neural network. In the training, the optimizer is run for 200 epochs with batch size of 1001 (corner-cube positions). The loss mean-squared error reduces to value corresponding to 0.3 mm in predicting the position (Figure 10).

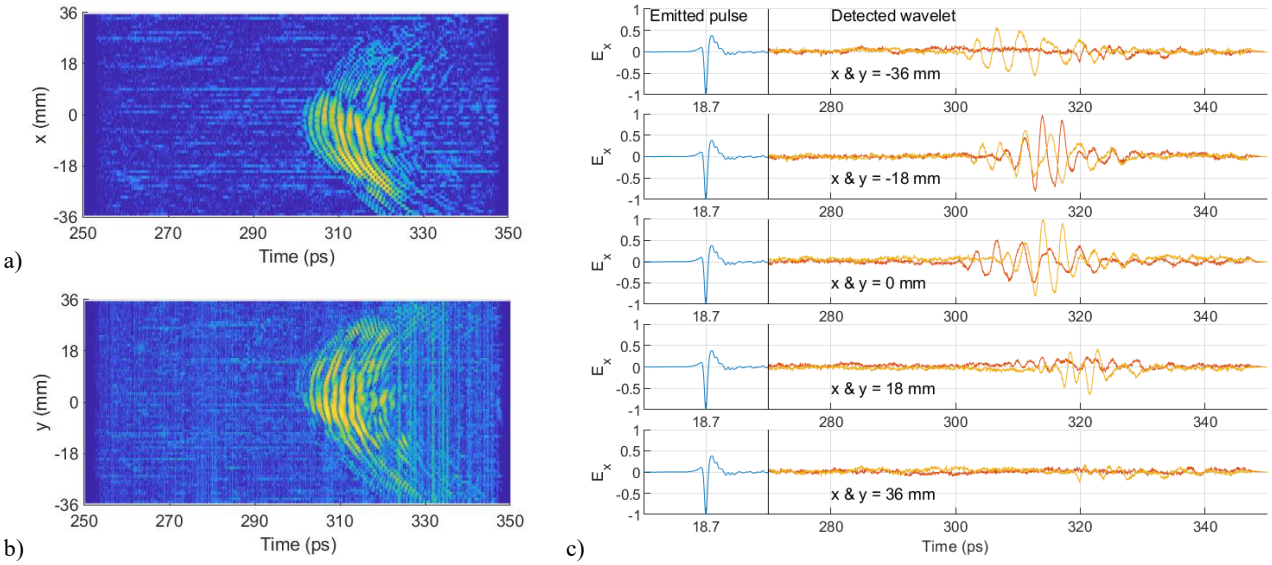

Figure 9. Detected wavelets on a) x- and b) y-axis when the corner-cube reflector is scanned in the 72-mm by 72-mm region of interest. c) Wavelets in along x- (red) and y-cuts (yellow) are shown in comparison to the emitted pulse (blue).

Table 2. Keras summary of the topography of the fully-connected neural network.

Layer (type)	Output Shape	Param #
dense (Dense)	(None, 1381)	1908542
dense_1 (Dense)	(None, 1381)	1908542
dense_2 (Dense)	(None, 1381)	1908542
dense_3 (Dense)	(None, 2)	2764
Total params: 5,728,390		
Trainable params: 5,728,390		
Non-trainable params: 0		

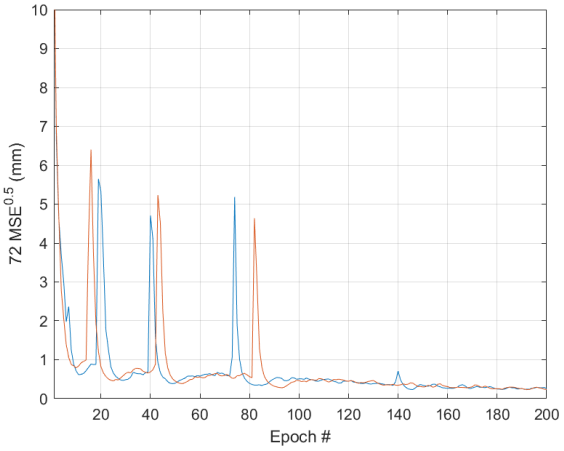

Figure 10. Loss in training the neural network for the two cases. The difference in loss is due to minute difference in the distributions of the training data. From Epoch #1 until #200 the training accuracy improves from more than 10 mm down to 0.3 mm.

The predicted corner-cube positions along with the ground truth are shown in Figure 11. Two distributions are shown: Case #1) corner cube in random positions in the region of interest and Case #2) random positions along x- and y-axis. The accuracy of the prediction is the best close to the center of the region of interest corresponding to the area where the detected wavelet amplitude (SNR) is at maximum. The average error of the position prediction is 0.5 mm for the Case #1 and 0.8 mm for the Case #2, respectively. The maximum error is 8 and 12 mm for Case #1 and #2, respectively.

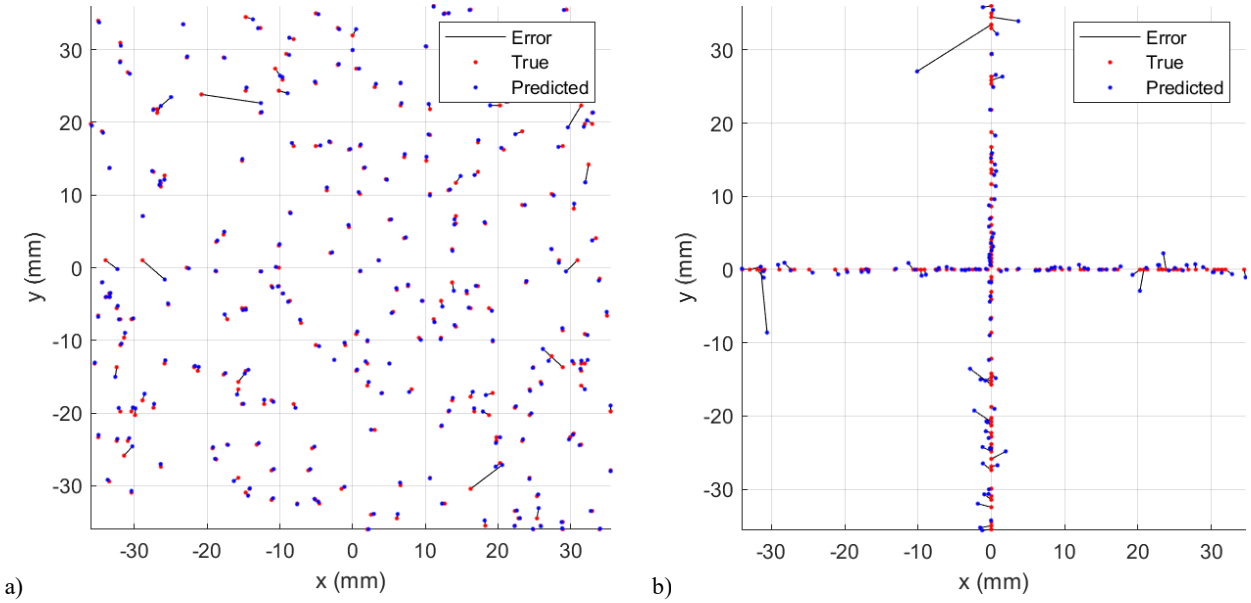

Figure 11. Predicted positions for corner cube located randomly a) in the region of interest and b) along the x- and y-axis in the region of interest. Red dots show the true position and blue dots show the prediction. The black lines connect the predictions to the true positions.

4. CONCLUSIONS

We have presented a new localization method leveraging the broad bandwidth of a terahertz time-domain spectrometer. A dispersive hologram transforms incident pulses into wavelets that interrogate the region of interest in a quasirandom fashion. Hybrid simulations combining the finite-difference and physical optics time-domain methods confirm that the hologram has suitable directivity ensuring that the majority of the incident energy propagates in to the region of interest while maintaining sufficient dispersion. The performance of the hologram is evaluated by a corner-cube scans in the region of interest. The loss in the propagation path is dominated by free-space loss and the efficiency of the beam splitter, which indicates that there is a safe link-budget marging: A submillimeter-wave transceiver can have 90-120 dB dynamic range clearly exceeding the loss.

We have trained a fully-connected deep neural network to predict the position of a corner-cube reflection based on the detected wavelets. We recognize that developing a neural network for real-life scenario requires significant amount of data in various environments. However, the initial results show that the prediction accuracy is of the order of a wavelength for the majority of the interrogated positions. This is achieved with relatively modest neural-network topography. The great benefit of our proposed method is that, effectively, 2-dimensional beamsteering is achieved without moving quasioptical components or electrically controlled phase shifters. Further, the emitter and detector count is limited to one.

With suitable training data, the dispersive hologram combined to broadband transceiver and neural network can produce real-time images from the region of interest, too. While our current setup allows only small-scale testing, we believe that scale-up to standoff submillimeter-wave screening application is straight forward and feasible.

5. ACKNOWLEDGEMENTS

This work is supported by the Academy of Finland through ADENN project.

REFERENCES

[1] K. B. Cooper, R. J. Dengler, N. Llombart, B. Thomas, G. Chattopadhyay, and P. H. Siegel, "THz imaging radar for standoff personnel screening," *IEEE Transactions on Terahertz Science and Technology*, vol. 1, no. 1, pp. 169-182, 2011.

[2] D. A. Robertson, D. G. MacFarlane, R. I. Hunter, S. L. Cassidy, N. Llombart, E. Gandini, T. Bryllert, M. Ferndahl, H. Lindström, J. Tenhunen, H. Vasama, J. Huopana, T. Selkälä, and A. J.Vuotikka, "A high frame rate, 340 GHz 3D imaging radar for security," *Proceedings of IEEE Radar Conference*, Oklahoma City, US, 2018, pp. 55-60.

[3] D. M. Sheen, D. L. McMakin, and T. E. Hall, "Three-dimensional millimeter-wave imaging for concealed weapon detection," *IEEE Transactions on Microwave Theory and Techniques*, vol. 49, no. 9, pp. 1581-1592, 2001.

[4] T. F. Gallacher, D. A. Robertson, and G. M. Smith, "The photo-injected Fresnel zone plate antenna: Optoelectronic beam steering at mm-wave frequencies," *IEEE Transactions on Antennas and Propagation*, vol. 61, no. 4, pp. 1688-1696, 2013.

[5] A. Kannegulla, Z. Jiang, S. Rahman, P. Fay, H. G. Xing, L.-J. Cheng, and L. Liu, "Coded-aperture imaging using photo-induced reconfigurable aperture arrays for mapping terahertz beams," *IEEE Transactions on Terahertz Science and Technology*, vol. 4, no. 3, pp. 321-327, 2014.

[6] M. F. Imani, J. N. Gollub, O. Yurduseven, A. V. Diebold, M. Boyarsky, T. Fromenteze, L. Pulido-Mancera, T. Sleasman, and D. R. Smith, "Review of metasurface antennas for computational microwave imaging," *IEEE Transactions on Antennas and Propagation*, vol. 68, no. 3, pp. 1860-1875, 2020.

[7] "TERA15-TX-FC, TERA15-RX-FC, Fiber-coupled photoconductive antenna", 9th April 2020, https://www.menlosystems.com/products/thz-antennas-and-components/tera15-fc/

[8] D. A. Robertson, *Private Communications*, Scotland, U.K., University of St Andrews, 2016.

[9] P. M. Johansen, "Time-domain version of the physical theory of diffraction," *IEEE Transactions on Antennas and Propagation*, vol. 47, no. 2, pp. 261-270, 1999.

[10] F. Le Bolzer, R. Gillard, J. Citerne, V. F. Hanna, and M. F. Wong, "An hybrid formulation combining FDTD and TDPO," *IEEE Antennas and Propagation Society International Symposium*, Atlanta, US, 1998, pp. 952-955.

[11] C. L. Bennett and G. F. Ross, "Time-domain electromagnetics and its applications," *Proceedings of the IEEE*, vol. 66, no. 3, pp. 299-318, 1978.

[12] "Keras Documentation", 9th April 2020, https://keras.io/

[13] D. P. Kingma, and J. Ba, "Adam: A method for stochastic optimization," *arXiv preprint*, arXiv:1412.6980, 2014.